RESEARCH ARTICLE

Loss of TREM2 diminishes CAA despite an overall increase of amyloid load in Tg-SwDI mice

Rui Zhong[1] | Yingzheng Xu[2,3] | Jesse W. Williams[2,3] | Ling Li[1]

[1]Department of Experimental and Clinical Pharmacology, University of Minnesota, Minneapolis, Minnesota, USA

[2]Center for Immunology, University of Minnesota, Minneapolis, Minnesota, USA

[3]Department of Integrative Biology and Physiology, University of Minnesota, Minneapolis, Minnesota, USA

Correspondence
Ling Li, Department of Experimental and Clinical Pharmacology, University of Minnesota, 2001 6th Street SE, McGuire Translational Research Facility (MTRF) 4-208, Minneapolis, MN 55455, USA.
Email: lil@umn.edu

Abstract

INTRODUCTION: The microglial receptor triggering receptor expressed on myeloid cells 2 (TREM2) is a major risk factor for Alzheimer's disease (AD). Experimentally, *Trem2* deficiency affects parenchymal amyloid beta (Aβ) deposition. However, the role of TREM2 in cerebrovascular amyloidosis, especially cerebral amyloid angiopathy (CAA), remains unexplored.

METHODS: Tg-SwDI (SwDI) mice, a CAA-prone model of AD, and *Trem2* knockout mice were crossed to generate SwDI/TWT, SwDI/THet, and SwDI/TKO mice, followed by pathological and biochemical analyses at 16 months of age.

RESULTS: Loss of *Trem2* led to a dramatic decrease in CAA and microglial association, despite a marked increase in overall brain Aβ load. Single nucleus RNA sequencing analysis revealed that in the absence of *Trem2*, microglia were activated but trapped in transition to the fully reactive state, with distinct responses of vascular cells.

DISCUSSION: Our study provides the first evidence that TREM2 differentially modulates parenchymal and vascular Aβ pathologies, offering significant implications for both TREM2- and Aβ-targeting therapies for AD.

KEYWORDS
Alzheimer's disease, cerebral amyloid angiopathy, cerebrovascular cells, microglia, triggering receptor expressed on myeloid cells 2

Highlights

- Triggering receptor expressed on myeloid cells 2 (TREM2) differentially modulates brain parenchymal and vascular amyloidosis.
- Loss of *Trem2* markedly reduces cerebral amyloid angiopathy despite an overall increase of amyloid beta load in Tg-SwDI mice.
- Microglia are trapped in transition to the fully reactive state without *Trem2*.
- Perivascular macrophages and other vascular cells have distinct responses to *Trem2* deficiency.
- Balanced TREM2-targeting therapies may be required for optimal outcomes.

1 | BACKGROUND

Triggering receptor expressed on myeloid cells 2 (TREM2) is expressed predominantly on microglia in the brain. Recent genome-wide association studies have identified TREM2 as a major genetic risk factor for Alzheimer's disease (AD).[1,2] TREM2 is a key regulator of microglial functions in normal aging and AD.[3] In transgenic mouse models, *Trem2* deficiency affects cerebral amyloid beta (Aβ) deposition, a neuropathological hallmark of AD, although the direction of the impact is sometimes inconsistent, depending on the stages of the development of Aβ pathology.[4–7] Nevertheless, it has been consistently observed that Aβ plaque-associated microgliosis is reduced regardless of the stages of Aβ pathology in the absence of *Trem2*, and transcriptomic studies have unveiled that *Trem2*-null microglia fail to switch to a disease-associated, reactive phenotype, leading to diffused amyloid plaques in the parenchyma.[4–10] However, the role of TREM2 in cerebrovascular amyloidosis, particularly cerebral amyloid angiopathy (CAA), remains unexplored.

CAA, characterized by Aβ deposition in the cerebrovascular basement membrane, is a common pathological feature of brains with AD.[11] It triggers cerebrovascular inflammation, hemorrhages, microinfarcts, and cognitive impairment.[12] AD subjects with CAA show a more rapid cognitive decline than those without CAA.[13] Moreover, CAA-related adverse effects hamper the development of Aβ-targeting immunotherapies, currently the most successful class of disease-modifying therapies for AD.[14] Compelling evidence indicates that CAA constitutes the underlying cause of amyloid-related imaging abnormalities (ARIAs), one of the main adverse events associated with anti-Aβ immunotherapies.[15] Thus, a better understanding of cerebrovascular amyloidosis not only elucidates the pathogenesis of CAA per se but also facilitates the development of safe and efficacious therapies for AD.

Aβ is produced by the sequential cleavage of amyloid precursor protein (APP) by β-secretase (BACE1) followed by γ-secretase.[16] Aβ40 and Aβ42 are the two most abundant products of the cleavage, constituting the main species in amyloid pathology in AD brains. Various point mutations in APP have been identified to cause familial AD, including the Swedish mutation (K670N/M671L),[17] while several other mutations cause familial CAA, including Dutch E22Q and Iowa D23N.[18,19] Although Aβ40 and Aβ42 are the primary constituents of both CAA and parenchymal plaques, Aβ40 is more vasculotropic than Aβ42 and accumulates largely along blood vessels to form fibrillar CAA, whereas Aβ42 mainly forms dense fibrillar cores of the parenchyma plaques.[20,21] Growing evidence suggests that cerebral vascular dysfunction precedes the buildup of amyloid plaques and tau tangles that eventually lead to cognitive deficits and AD.[22,23] An early presence of CAA at the basement membrane of the vessel wall caused by insufficient clearance of excess Aβ via the perivascular pathway is thought to impair the blood–brain barrier (BBB) function.[24,25] However, how vascular Aβ interacts with the neurovascular unit and other adjacent cell types remains elusive. While recent studies highlight the importance of microglia in the pathogenesis of CAA,[26–28] the specific role of TREM2 in CAA has not been explored.

RESEARCH IN CONTEXT

1. **Systematic review**: The authors searched published literature for both experimental and clinical evidence on the connection between triggering receptor expressed on myeloid cells 2 (TREM2) and Alzheimer's disease (AD) and cerebral amyloid angiopathy (CAA). While TREM2 is an established genetic risk factor for AD and several studies have used *Trem2* knockout models to investigate the role of TREM2 in AD pathogenesis, none has studied whether TREM2 specifically affects CAA, a major pathology of AD.

2. **Interpretation**: *Trem2* deficiency dramatically decreases CAA despite an overall increase of brain amyloid beta (Aβ) load, with unique responses of microglia and vascular cells, in a CAA-prone mouse model of AD. These findings provide the first evidence that TREM2 differentially modulates parenchymal and vascular Aβ pathologies, offering significant implications for TREM2- and Aβ-targeting therapies against AD.

3. **Future directions**: Future studies are warranted to investigate the impact of TREM2 on vascular amyloidosis in other models, and determine whether modulating TREM2 expression/activities mitigates CAA-related adverse effects associated with immunotherapies for AD.

Therefore, the current study aimed to determine the impact of *Trem2* deficiency on CAA and the neurovascular components in addition to parenchymal Aβ deposition in the brain. We used a well-characterized transgenic mouse model of CAA/AD, Tg-SwDI or SwDI,[29] carrying both the familial Swedish and Dutch/Iowa mutations that drive the CAA formation. SwDI mice develop age-dependent diffused parenchymal Aβ plaques and CAA in various brain regions.[29] We generated the SwDI/Trem2 mouse line by breeding SwDI with *Trem2*–/– mice [30] and studied the mice at 16 months of age. We found that loss of *Trem2* led to a drastic diminishment of CAA, along with reduced CAA-associated microgliosis, despite a marked exacerbation of parenchymal Aβ deposition. Single nucleus transcriptomic analyses revealed that interactions of microglia, perivascular macrophages, and other vascular cells contributed to the shift from CAA to parenchymal plaques in *Trem2*-deficient mice. These findings demonstrate a previously unrecognized differential role of TREM2 in modulating parenchymal and vascular amyloid pathology.

2 | METHODS

2.1 | Animals

Tg-SwDI (SwDI) mice (C57BL/6-Tg[Thy1-APPSwDutIowa]BWevn/ Mmjax) have been described previously,[29] and *Trem2*-knockout (TKO)

mice [30] were generously provided by Dr. Marco Colonna at the Washington University in St. Louis. The SwDI/Trem2 line was generated by the two-step breeding of SwDI mice with TKO mice, producing six genotypes: SwDI;*Trem2*–/– (SwDI/TKO), SwDI;*Trem2* +/- (SwDI/THet), SwDI;*Trem2*+/+ (SwDI/TWT), *Trem2*–/– (TKO), *Trem2* +/- (THet), and wild type (WT). Mice carrying the SwDI transgene were used in the present study. Littermates were used whenever possible, and both males and females were included. All animal experiments were reviewed and approved by the Institutional Animal Care and Use Committee of the University of Minnesota (protocols # 1908-37310A and 2207-40221A).

2.2 | Immunohistochemical, immunofluorescent, and histochemical staining

Immunohistochemistry experiments were conducted as previously described.[31] Briefly, the posterior half of the mouse brains were collected and post-fixed with 4% paraformaldehyde for 48 hours. Fifty-micrometer coronal sections were obtained using a vibratome (Leica Microsystems Inc.). For the immunohistochemical staining, the VECTASTAIN ABC kit (Vector Laboratories, PK-4002) was used following the manufacturer's protocol. For immunofluorescent staining, sections were washed with phosphate-buffered saline (PBS) before blocking (5% normal donkey serum and 0.5% Triton X-100 in PBS) for 1 hour at room temperature followed by overnight incubation with primary antibodies. Sections were then washed and incubated with secondary antibodies for 3 hours at room temperature. After PBS washes, sections were mounted onto glass slides and sealed in the Vectashield HardSet antifade mounting medium (Vector Laboratory). Methoxy-X04 (Tocris 4920) staining was conducted as previously described,[32] after the incubation of secondary antibodies. The primary antibodies used include anti-Aβ 6E10 (BioLegend 803002), anti-glial fibrillary acidic protein (GFAP; Dako Z0334), anti-ionized calcium-binding adapter molecule 1 (IBA1; Wako 019-19741), and anti-cluster of differentiation 31 (CD31; R&D AF3628). The secondary antibodies for immunofluorescence include donkey anti-mouse immunoglobulin G (IgG) Alexa Fluor 568, anti-rabbit IgG Alexa Fluor 488 and 647, anti-rat IgG Alexa Fluor 488 and 647, and anti-goat IgG Alexa Fluor 488 (Invitrogen).

2.3 | Optical and fluorescent imaging and quantification

Four consecutive sections that were 350 μm apart and two that were 300 μm apart were selected for immunohistochemical and immunofluorescent quantifications, respectively, as described previously with some modifications.[31,33] Briefly, for optical imaging, the images were acquired with a 4x objective lens and subsequently stitched with ImageJ/FIJI. The immunoreactivity of Aβ, IBA1, and GFAP in the cortex, hippocampus, and thalamus of the mouse brains was quantified with individual 4x images acquired with Image-Pro Plus (MediaCybernet-

ics). These images were converted to 16-bit grayscale on Image J/FIJI and subsequently quantified with the same threshold. A minimum size of 30 μm^2 was applied to filter out small non-specific staining. For fluorescent imaging, sections were imaged using the Keyence all-in-one fluorescent microscope (Keyence, BZ-X810). The entire section was scanned under a 10x objective lens and a stitched image was produced in the Keyence Analysis software. Similar approaches were applied for the quantifications and representative images of CAA and associated microglia. For quantifications, images were taken under a 20x objective with a field of view (FOV) of 720 μm x 540 μm. For representative images, a z-stack of images (8 μm $\pm$ 0.12 μm) with a z-step size of 0.2 um was taken under a 100x oil objective lens using the multi-stack module. At least six 20x images per animal from the same region in the thalamus were used for quantifications, and the staining was quantified per FOV with regions of interest (ROIs) to exclude non-target staining using ImageJ/FIJI. For the CAA-associated microglia quantification, the microglial association was defined as within 5 μm of CAA immunostaining, and ROIs were selected around CAA and expanded 5 μm in ImageJ/FIJI. For X04+ plaque density quantifications, fluorescent images were converted to 16-bit on grayscale, and gray values were quantified as a readout for fluorescent intensity representing plaque density. The same threshold was applied within each channel per experiment, and the rolling ball method was used to reduce background staining. Results were averaged across the sections for each animal.

2.4 | Whole mouse brain processing/clearing, immunostaining, and 3D imaging

Whole mouse brains were processed following the SHIELD protocol.[34] Samples were cleared for 1 day at 42°C with SmartBatch+ (LifeCanvas Technologies), a device using stochastic electrotransport.[35] Cleared samples were then actively immunolabeled using SmartBatch+ (LifeCanvas Technologies) based on eFLASH technology integrating stochastic electrotransport [35] and SWITCH.[36] Each brain sample was stained with primary antibodies, 5 μg of mouse anti-Aβ antibody (Encor, #MCA-AB9), 5 μg of rabbit anti-IBA1 monoclonal antibody (Cell Signaling Technologies, #17198S), and 10 μg of goat anti-CD31 (R&D Systems, #AF3628) followed by fluorescently conjugated secondary antibodies in 1:2 (primary:secondary) molar ratios (Jackson ImmunoResearch). After active labeling, samples were incubated in EasyIndex (LifeCanvas Technologies) for refractive index matching (RI = 1.52) and imaged at either 3.6X or 15X with a SmartSPIM axially-swept light sheet microscope (LifeCanvas Technologies).

2.5 | Immunoblotting

The experimental procedures for protein assay and immunoblotting have been previously described.[31,33] Briefly, protein concentrations from total brain tissue homogenates were determined by the Bradford assay (Thermo Fisher 23246). Proteins were then separated by

12% sodium dodecyl-sulfate polyacrylamide gel electrophoresis and transferred to polyvinylidene fluoride membranes. After blocking, the membranes were incubated in primary antibodies overnight. The primary antibodies used include beta-secretase 1 (BACE1; Invitrogen PA1-757), GFAP (Aves labs), IBA1 (Wako 016-20001), glyceraldehyde 3-phosphate dehydrogenase (Invitrogen AM4300), and tubulin (Sigma-Aldrich T5198). Subsequently, the membranes were incubated with horseradish peroxidase-conjugated secondary antibodies, followed by incubation in the Clarity Western enhanced chemiluminescent substrate (Bio-Rad) for signal detection using the iBright Western Blot Imaging System (Thermo Fisher). Densitometric analysis was performed using the ImageJ software.

2.6 | Aβ species-specific enzyme-linked immunosorbent assay

The anterior half of the cortical hemisphere was homogenized for immunoblot analysis (see above) and Aβ enzyme-linked immunosorbent assay (ELISA). For the ELISA fraction, homogenized samples were further sequentially separated into the carbonate-soluble and guanidine-soluble fractions as previously described.[31,33] The levels of Aβ40 and Aβ42 were measured using Aβ40- and Aβ42-specific ELISA kits (Invitrogen KHB3481 and KHB3441) according to the manufacturer's protocol.

2.7 | Nuclei isolation from flash-frozen mouse brain tissue

Nuclei from six female mouse brain cortical tissues (three for each genotype) were isolated following the 10x Genomics Demonstrated Protocol (CG000375; Nuclei Isolation from Complex Tissues for Single Cell Multiome ATAC + Gene Expression Sequencing), with the following modifications: the NP40 Lysis Buffer was used at a 20X dilution, tissue dissociation was performed on the gentleMACS Octo Dissociator with Heaters (Miltenyi Biotec, Bergisch Gladbach) using a modified version of the 4C_nuclei_1 program, and no nuclei permeabilization was performed. Nuclei were not sorted before capture.

2.8 | Single nucleus RNA sequencing library construction using the 10x Genomics Chromium platform

Single nucleus RNA sequencing (snRNA-seq) libraries were prepared per the Single Cell 3′ v3.1 Reagent Kits User Guide (10x Genomics) using the 10x Genomics Chromium Controller, X, or Connect. Barcoded sequencing libraries were quantified by quantitative polymerase chain reaction using the Collibri Library Quantification Kit (Thermo Fisher Scientific). Libraries were sequenced on a NovaSeq 6000 (Illumina) as per the Single Cell 3′ v3.1 Reagent Kits User Guide, with a sequencing depth of ≈ 40,000 reads/nucleus. The estimated number of nuclei sequenced from individual samples ranged from 5700 to 8100.

2.9 | Initial data analysis

The demultiplexed raw reads were aligned to the transcriptome using STAR (version 2.5.1) [37] with default parameters, using mouse mm10 transcriptome reference from Ensembl version 84 annotation, containing all protein-coding and long non-coding RNA genes. Expression counts for each gene in all samples were collapsed and normalized to unique molecular identifier (UMI) counts using Cell Ranger software version 4.0.0 (10X Genomics). The result is a large digital expression matrix with cell barcodes as rows and gene identities as columns.

2.10 | Count matrix generation and preprocessing

Sequencing read alignment was performed using cellranger (v6.1.2) count pipeline, where FASTQ files generated from cellranger mkfastq were mapped to a murine reference transcriptome (https://cf.10xgenomics.com/supp/cell-exp/refdata-gex-mm10-2020-A.tar.gz). cellranger count output containing filtered count matrix was adopted into R by Seurat (v4.0.1)[38] Read10X function. Cells with < 200 total feature reads or possessing > 25% mitochondrial mRNA content were removed as potential empty or apoptotic cells. Prior to snRNA-seq dataset integration, the DoubletFinder package[39] was used to further refine doublet detection. Filtered snRNA-seq objects were then merged and followed by normalization and scaling using Seurat NormalizeData and ScaleData functions with default parameters. Calculation of the top 3000 features that exhibit significant cell-to-cell variations was done by the FindVariableFeatures function. Overall, 23,483 genes and 36,000 nuclei remained after filtering.

2.11 | Integration, clustering, and cell type annotation

First, linear dimensional reduction and principal component analysis (PCA) were performed on the merged dataset that passed previous preprocessing filters. The principal components (PCs) were ranked based on explained variance of each PC to determine the most meaningful number of PCs (nPCs), which was reflected by the turning point in an elbow diagram by Elbowplot. Collectively, the top 20 PCs were able to cover the most meaningful PCs. Then, batch effects were corrected using the Harmony package[40] RunHarmony function and projected dataset in UMAP and tSNE embeddings. This integration pipeline was adopted from Seurat and Harmony vignettes. To avoid manual annotation of a clustered dataset that may involve biased opinions, a computational approach using the map_sampling function of scrattch.hicat package[41] was implemented. Cells in our dataset were bootstrap-mapped with a mouse cortex RNA-seq dataset reported by Tasic et al.[42] The final cell type predictions were evaluated by the authors using reported marker genes. Initial clustering of all nuclei was performed using a resolution of 0.6. Further rec-lustering of vascular cells, microglia, and macrophages used resolutions of 0.6, 0.3, and

0.4, respectively. Over-clustered populations were refined and merged according to the signature gene expressions.

2.12 | Differential gene expression and pathway analysis

Differential expression (DE) analysis was performed using Seurat Find-Markers and FindAllMarkers functions. Log fold change threshold was set to 0 to avoid gene filtering by the DE function. The fgsea function of the fgsea package was used to profile pathway analysis. The Molecular Signature Database (MSigDB) containing all known annotated gene sets was imported to be used with fgsea. Then, log fold change values generated from DE algorithms were added to their corresponding gene symbols. Next, the named array was rank-ordered in fgsea, and MSigDB gene sets were subsequently mapped onto the ranked array. Statistical significance of the pathways was determined as adjusted p value < 0.1. The classification of significant pathways (Table S1 in supporting information) was based on keywords identified by the authors for each respective class, and was manually examined for errors. The raw snRNA-seq datasets are available in the Gene Expression Omnibus repository (GEO Series accession number GSE244286).

2.13 | Statistical analysis

Statistical tests, including one-way analysis of variance with Tukey post hoc test and Student's t-test, were carried out with GraphPad Prism 9, and data are presented in boxplots. The box extends from the 25th to 75th percentiles and the whiskers from the minimum and to the maximum value. A p value < 0.05 was considered significant.

3 | RESULTS

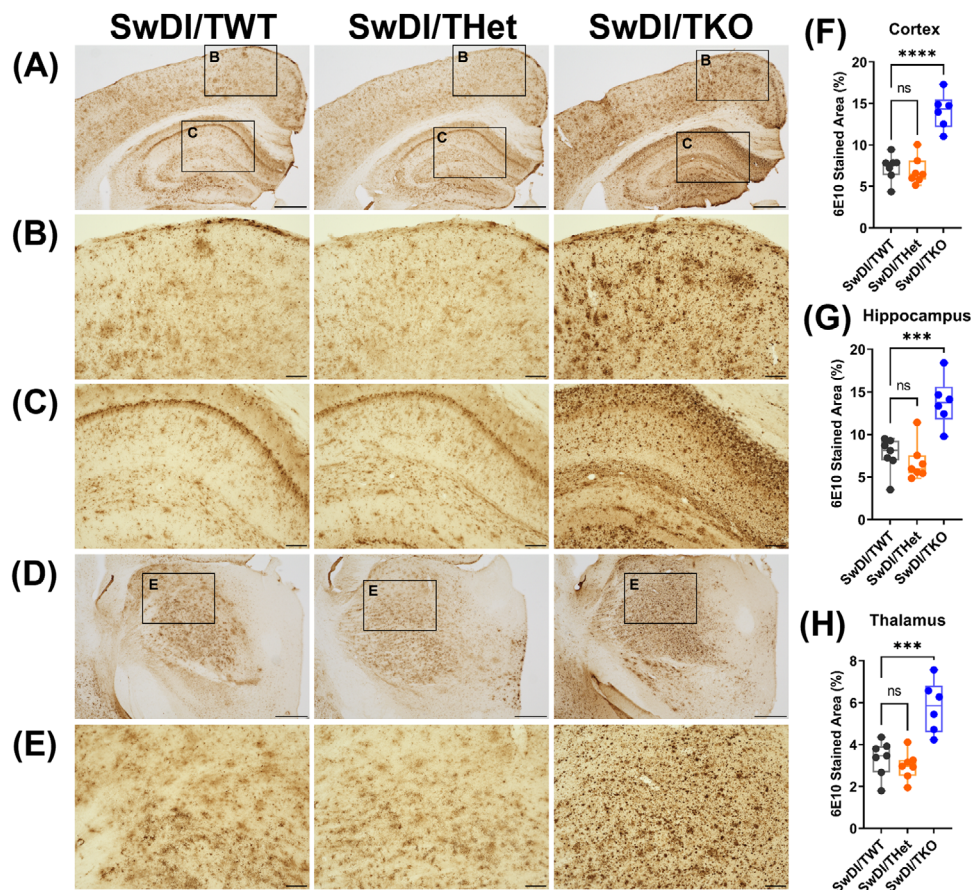## 3.1 | *Trem2* deletion exacerbates overall amyloid deposition and production

The impact of *Trem2* deficiency on amyloid pathology was evaluated in a cohort of 16-month-old SwDI/Trem2 mice matched by sex and genotype. Immunohistochemical (IHC) analyses showed that amyloid deposition measured by 6E10 immunoreactivity was significantly exacerbated in SwDI/TKO compared to SwDI/TWT mice in the cortex (Figure 1A-B), hippocampus (Figure 1A, C), and thalamus (Figure 1D-E). Quantifications of 6E10 immunoreactive area showed an $\approx$ 2-fold increase in the amyloid load in SwDI/TKO compared to SwDI/TWT in all three quantified regions (Figure 1F-H). Subanalysis of the plaque size distribution showed the same differences when plaques were divided into small ($< 20\,\mu m$), medium ($20-40\,\mu m$), and large ($> 40\,\mu m$) in cortical images (Figure S1A-C). Notably, there was no significant difference between SwDI/TWT and SwDI/THet mice, indicating that one copy of *Trem2* is sufficient to keep the amyloid pathology at bay.

To investigate the underlying reasons for the increase in amyloid deposition, Aβ40- and Aβ42-specific quantitative ELISA were performed. In SwDI mice, Aβ40 accumulates more aggressively than Aβ42 in the brain parenchyma and cerebral vasculatures driven by the Dutch and the Iowa familial AD mutations.[29] Therefore, Aβ40 and Aβ42 levels were evaluated in the carbonate soluble and insoluble (guanidine-soluble) fractions. As expected, Aβ40, Aβ42, and the Aβ40/Aβ42 ratio all significantly increased in SwDI/TKO mice compared to SwDI/TWT in both carbonate soluble and insoluble fractions (Figure 2A-D). In addition, consistent with the immunostaining results (Figure 1), there was no significant difference between SwDI/TWT and SwDI/THet mice (Figure 2A-D). Thus, subsequent analyses focused on the comparisons between SwDI/TWT and SwDI/TKO groups. Immunoblot analysis showed a significant increase in BACE1 level in the SwDI/TKO group compared to SwDI/TWT (Figure 2E-F), suggesting that enhanced amyloidogenic processing of APP contributes to the elevated levels of Aβ40 and Aβ42 in SwDI/TKO mice.

3.2 | *Trem2* deletion diminishes CAA despite an increase in total fibrillar Aβ

The elevated Aβ40/Aβ42 ratio in the absence of TREM2 (Figure 2D) suggested a potential increase in CAA. To quantify CAA, methoxy-X04 (X04) was used to stain fibrillary Aβ co-stained with CD31 to label the vascular endothelium to aid the visualization of CAA. The results showed that in the cortical area, the X04-stained amyloid fibrils/compact plaques were minimal in SwDI/TWT mice (Figure 3A-B) despite the abundance of 6E10+ immunostaining (Figure 1), confirming earlier reports that the parenchymal amyloid deposits are diffuse in nature resulting from the high level of vasculotropic Aβ40 in SwDI mice.[29,43] The same studies also reported CAA largely present in the thalamus and subiculum, although with minimal X04+ plaque load as in SwDI/TWT mice (Figure 3A-B, F). In contrast, total X04$^+$ amyloid fibrils were markedly increased in the cortex, hippocampus, and thalamus of SwDI/TKO mice (Figure 3A-E, Figure S2A-B in supporting information), corresponding to the increase in total amyloid deposition by 6E10-immunostaining (Figure 1). However, intriguingly, there was a marked decrease of CAA in *Trem2*-deficient mice in the thalamus (Figure 3F-G) where CAA was most abundant, indicating that despite the increase in Aβ40/Aβ42 or the overall increase of total Aβ (Figure 2), loss of *Trem2* led to diminished CAA in SwDI mice. To confirm this unexpected finding, whole brain hemispheres of SwDI/TKO and SwDI/TWT littermates were subjected to brain clearing for 3D imaging. The brains were processed via SHIELD, SmartClear, immunostaining procedures to label Aβ plaques, microglia (IBA1), and blood vessels (CD31) and imaged using a SmartSPIM axially swept light sheet microscope. The results clearly showed a dramatic decrease of CAA in the SwDI/TKO brain compared to the SWDI/TWT brain, despite significantly increased overall Aβ load in SwDI/TKO (Figure 3H). To further understand if the compactness of fibrillar amyloid changes after a shift from CAA to diffused plaques when *Trem2* is deleted, the fluorescent intensity of each individual X04$^+$ amyloid staining in the thalamus was analyzed. The results

FIGURE 1 *Trem2* deletion exacerbates total amyloid deposition in SwDI mice. A, D, Representative images of the immunohistochemical staining of amyloid by 6E10 in (A) cortex, hippocampus, and (D) thalamus in SwDI/TWT ($n = 7$), SwDI/THet ($n = 7$), and SwDI/TKO ($n = 6$) mice. Scale bars, 500 μm. B, C, E, Selected zoomed-in areas from the representative images of (B) cortex, (C) hippocampus, and (E) thalamus. Scale bars, 100 μm. F-H, Quantifications of the immunoreactive area of 6E10 in SwDI/TWT, SwDI/THet, and SwDI/TKO mice in (F) cortical, (G) hippocampal, and (H) thalamic regions, respectively. One-way analysis of variance and Tukey post hoc test. ***$p < 0.001$, ****$p < 0.0001$. ns, not significant.

showed a significant decrease in the average maximal intensity and an increase in the average minimal intensity in SwDI/TKO mice compared to SwDI/TWT (Figure S2C-D), indicating that *Trem2* deficiency reduced the core density of amyloid fibrils.

3.3 | *Trem2* deletion reduces microgliosis in the thalamus and decreases CAA-associated microglia

TREM2 plays a crucial role in regulating microglial activation and function, and loss of TREM2 modifies the response of microglia to Aβ. To assess the impact of *Trem2* deletion on microgliosis in SwDI mice, brain sections were subjected to IBA1 immunostaining. Interestingly, IHC analysis showed no changes in global microgliosis in SwDI/TKO compared to SwDI/TWT and SwDI/THet mice in the cortex or the hippocampus (Figure 4A, D-E), although microglial clustering was clearly reduced in the hippocampal CA1 stratum oriens region in SwDI/TKO mice (Figure S3A-B in supporting information). Intriguingly, microgliosis was significantly decreased in the thalamus of SwDI/TKO mice (Figure 4B-C, F). Immunoblot analysis of the corti-

cal homogenates also confirmed that IBA1 level was not significantly different between SwDI/TKO and SwDI/TWT mice (Figure 4G-H). Consistent with Aβ-staining results (Figure 1), no significant differences in IBA1 staining were found between SwDI/TWT and SwDI/THet. Therefore, SwDI/THet was not included in the following experiments assessing microglial pathology in the thalamus.

As Aβ deposits in the thalamus are predominantly CAA, brain sections were co-stained with X04 and IBA1 to determine whether the reduction of microgliosis corresponds to the reduction of CAA in this region. Indeed, X04 and IBA1 were completely co-localized in the thalamus of SwDI/TWT mice (Figure 4I), indicating the region-specific reduction of microgliosis in SwDI/TKO corresponds to the location of diminished CAA pathology. Consistently, CAA-associated microglia were significantly reduced in the thalamus of the SwDI/TKO compared to SwDI/TWT (Figure 4I-J), aligning with previous literature showing reduced plaque-associated microglia in other *Trem2*-deficient transgenic AD mouse models.[4–9,32,44] Additionally, microglia adopted a less reactive morphology with smaller soma and longer processes in SwDI/TKO than SwDI/TWT mice (Figure 4K). Together, these data suggest that the lack of TREM2 prevents microglia from switching
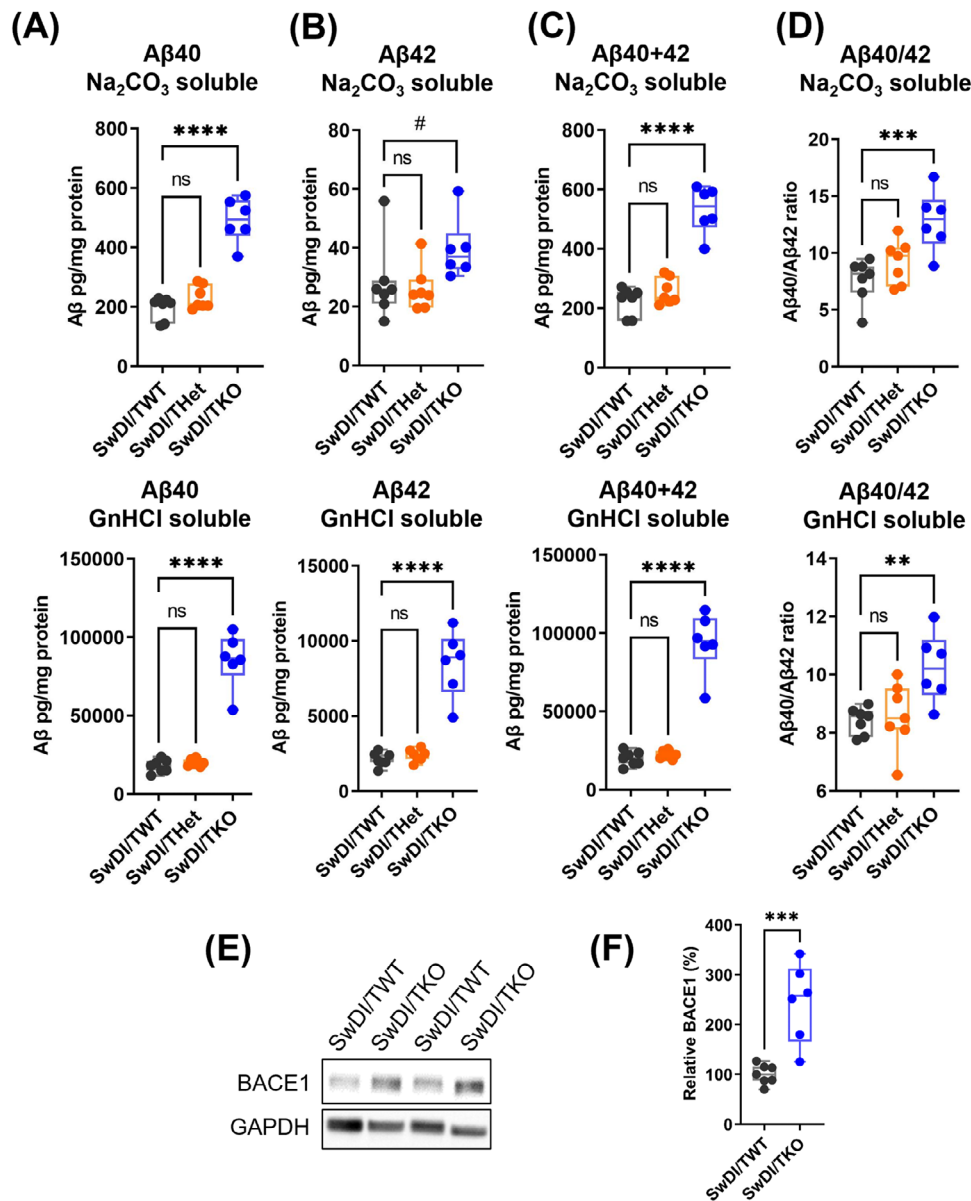
FIGURE 2 *Trem2* deletion elevates overall Aβ levels in SwDI mice and induces APP processing. A-D, ELISA on Aβ40 and Aβ42 in SwDI/TWT ($n = 7$), SwDI/THet ($n = 7$), and SwDI/TKO ($n = 6$) groups. The levels of (A) Aβ40 and (B) Aβ42, (C) total Aβ40 and Aβ42, and (D) the ratio of Aβ40/Aβ42 in both carbonate soluble and guanidine soluble fractions were all elevated in the SwDI/TKO mice whereas SwDI/THet mice showed no difference compared to SwDI/TWT. One-way analysis of variance and Tukey post hoc test. E-F, Immunoblot analysis of BACE1. Representative images of the BACE1 immunoblot (E) and the quantification of BACE1 normalized by GAPDH (F) showed a significant increase in BACE1 level in SwDI/TKO mice compared to SwDI/TWT mice. Unpaired Student's t-test, two-tail. #$p < 0.1$, **$p < 0.01$, ***$p < 0.001$, ****$p < 0.0001$. ns, not significant. Aβ, amyloid beta; APP, amyloid precursor protein; BACE1, β-secretase 1; ELISA, enzyme-linked immunosorbent assay; GAPDH, glyceraldehyde 3-phosphate dehydrogenase.

to a reactive state and impairs the ability of microglia to engage CAA.

3.4 | *Trem2* deletion aggravates cortical and hippocampal astrocytosis

Astrocytes, as well as microglia, respond to amyloidosis and regulate neuroinflammation. To assess the impact of *Trem2* deficiency on astro-

cytosis, brain sections of different genotypes of mice were subjected to GFAP immunostaining. The results showed that astrocytosis was significantly increased in cortical and hippocampal regions in SwDI/TKO compared to SwDI/TWT mice, whereas no change was seen in SwDI/THet mice (Figure 5A-C, E-F), consistent with overall Aβ deposition in these mice (Figure 1). The significant increase of GFAP in the cortex of SwDI/TKO mice was confirmed by immunoblot analysis of cortical homogenates from SwDI/TKO and SwDI/TWT mice (Figure 5H-I). Notably, there was no difference in GFAP immunoreactivity between
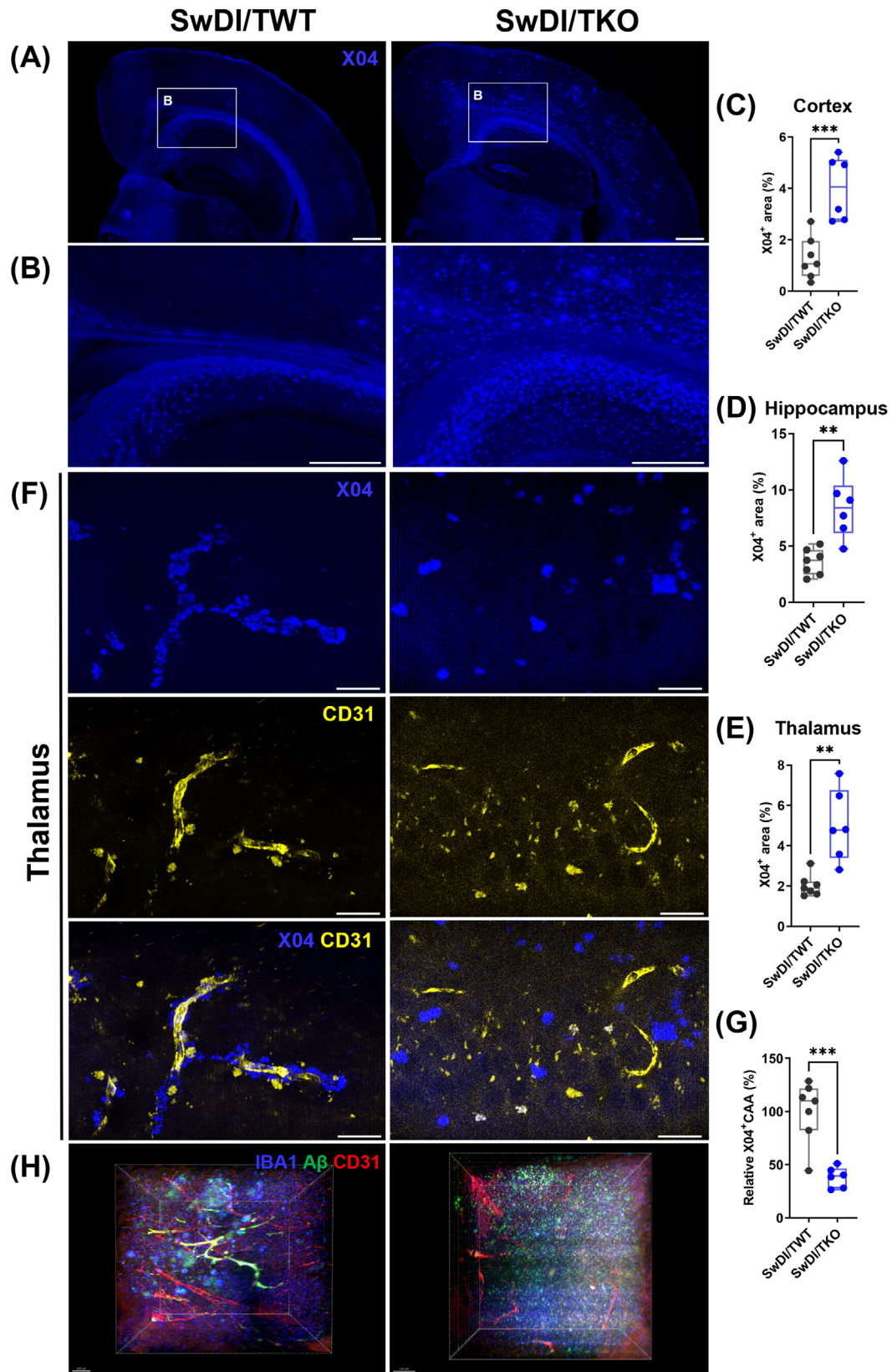
FIGURE 3 *Trem2* deletion decreases CAA despite an increase in total amyloid fibrils in SwDI mice. A, The representative stitched images of the fluorescent staining of methoxy-X04 under the 10x objective lens. Scale bars, 500 μm. B, Selected zoomed-in areas of (A). Scale bars: 300 μm. C-E, Quantifications of the X04+ stained area in SwDI/TWT (*n* = 7) and SwDI/TKO (*n* = 6) in (C) cortex, (D) hippocampus, and (E) thalamus, respectively. F, Representative images of CAA co-stained with capillaries (CD31) and amyloid fibrils (X04) in the thalamus. Scale bars: 20 μm. G, Quantification

SwDI/TWT and SwDI/TKO in the thalamus (Figure 5D, G), where CAA and microgliosis were significantly reduced in SwDI/TKO (Figures 3 and 4). These results suggest that astrocyte activation is independent of TREM2 and responds more to parenchymal Aβ deposition than to CAA.

3.5 | Single nucleus transcriptomic analysis reveals that microglia are trapped in transition in the absence of *Trem2*

To further investigate the molecular mechanisms underlying the pathological changes after *Trem2* deletion, snRNA-seq was performed using the frontal cortex tissues of SwDI/TWT and SwDI/TKO mice. After removing low-quality nuclei, transcriptional data from 36,660 nuclei were subjected to unsupervised clustering t-distributed stochastic neighbor embedding (t-SNE) in two dimensions. To avoid manual annotation of cell types, bootstrapping algorithms were applied to match cells in our dataset to mouse cortical cell types in a published dataset[42] to predict the cell types, namely oligodendrocyte precursor cells (OPCs), vascular cells, oligodendrocytes (oligo), inhibitory neurons, excitatory neurons, microglia, astrocytes, and macrophages (Figure 6A-D). The marker genes generated from these cell types were compared to reported marker genes[45–48] to confirm the cell type prediction (Figure 6B-C). For both genotypes, although there were some individual variations in relative fractions of cell types, overall there were no significant differences in representation of different cell types between SwDI/TWT and SwDI/TKO (Figure 6E-F).

Multiple AD studies have used *Trem2*-deficient models and demonstrated distinct reactive transcriptomic profiles in microglia that are *Trem2*-dependent, featuring genes present in disease-associated microglia (DAM). Therefore, the analysis was focused first on the microglia cluster (Figure 7A) comparing SwDI/TKO to SwDI/TWT, and 71 differentially expressed genes (DEGs) were identified, of which 58 were upregulated in SwDI/TKO (Figure 7B; Table S2 in supporting information). Among the DEGs, known DAM genes, including *Ctsd*, *Ctsb*, *Gnas*, and *APOE*, were upregulated in the SwDI/TKO group, while homeostatic microglial marker genes such as *Cx3cr1* were downregulated.[9,49,50] Notably, these DEGs have been reported to be responsible for the microglial transition from homeostatic stage to exclusively Stage 1 DAM (also known as the intermediate stage), which is *Trem2*-independent.[49] Correspondingly, there were no DEGs involved in the *Trem2*-dependent transition to Stage 2 DAM (Table S2). Pathway analysis on microglia unveiled an overwhelming upregulation of pathways mostly related to a reactive state of microglia in SwDI/TKO compared to SwDI/TWT, including protein syn-

thesis, cell death, energy production, and mitochondrial regulation, immune response, autophagy, and lipid biosynthesis and metabolism (Figure 7C). These findings indicate that microglia lacking *Trem2* adopted a stressed state in response to amyloidosis. However, as microglia were trapped in the intermediate Stage 1 of the DAM transition in the absence of TREM2, they were not sufficiently reactive to contain Aβ deposition, leading to an overall increase of amyloid pathology in SwDI/TKO mice.

Interestingly, further re-clustering of microglia uncovered two subclusters (0 and 1; Figure 7D-E), although the distribution of microglia between the two clusters was similar in SwDI/TWT and SwDI/TKO (Figure S4A in supporting information). Pathway analysis showed that the two subclusters of microglia have distinct functions. In microglia cluster 0, protein synthesis, mitochondria functions, and energy metabolism were among the most significantly enriched Gene Ontology (GO) pathways, while microglia cluster 1 was characterized mainly by immune functions including immune cell activation, phagocytosis, and cytokine production (Figure S4B). Compared to SwDI/TWT, *Trem2* deficiency enhanced the respective signature functions characterizing the microglial subclusters 0 and 1, demonstrating divergent contributions from microglia clusters 0 and 1 to the stressed microglial state in SwDI/TKO (Figure 7F).

3.6 | Perivascular macrophages are differentially activated in the absence of *Trem2*

In addition to microglia, TREM2 is also expressed in macrophages.[51] To understand the impact of *Trem2* deletion on macrophages in the context of amyloidosis in SwDI mice, further analysis was conducted for a small population of macrophages identified from cell type prediction (Figure 7G). The macrophages were re-clustered into three subpopulations (0, 1, and 2; Figure 7H). Cluster 0 covered the largest proportion of cells, characterized by perivascular macrophage (PVM) marker CD163 and Mrc1 (CD206[52,53]; Figure 7I). PVMs are a distinct population of resident brain macrophages characterized by close association with the cerebral vasculature. In AD, these vessel-associated macrophages are shown to exacerbate AD pathologies including CAA and neuroinflammation and contribute to the detrimental effect of Aβ in affecting cerebral blood flow.[54,55] There were two significant DEGs in SwDI/TKO versus SwDI/TWT: *Fkbp5*, crucial in AKT pathway regulation and NF-κB activation,[56,57] was upregulated; whereas *Malat1*, a non-coding RNA, was downregulated, as observed in microglia carrying the dysfunctional *Trem2*-R47H mutation.[58] Pathway analysis of cluster 0 (PVM) revealed that pathways related to protein synthesis and immune reaction are more enriched in SwDI/TKO (Figure 7J). In

---

of CAA, showing significant decrease of CAA in SwDI/TKO compared to SwDI/TWT. H, Representative 3D images of whole brain clearing and immunostaining with anti-Aβ, IBA1, and CD31 antibodies. While endothelial marker CD31 (red) and Aβ (green) co-stained CAA microvessels (yellow) are clearly seen in the thalamus image of SwDI/TWT, almost no CAA is visible in the thalamus image of SwDI/TKO, despite significantly more Aβ load (green) in SwDI/TKO. Scale bars, 200 μm. Unpaired Student's *t*-test, two-tail. **$p < 0.01$, ***$p < 0.001$. Aβ, amyloid beta; CAA, cerebral amyloid angiopathy; CD31, cluster of differentiation 31; IBA1, ionized calcium-binding adapter molecule 1.
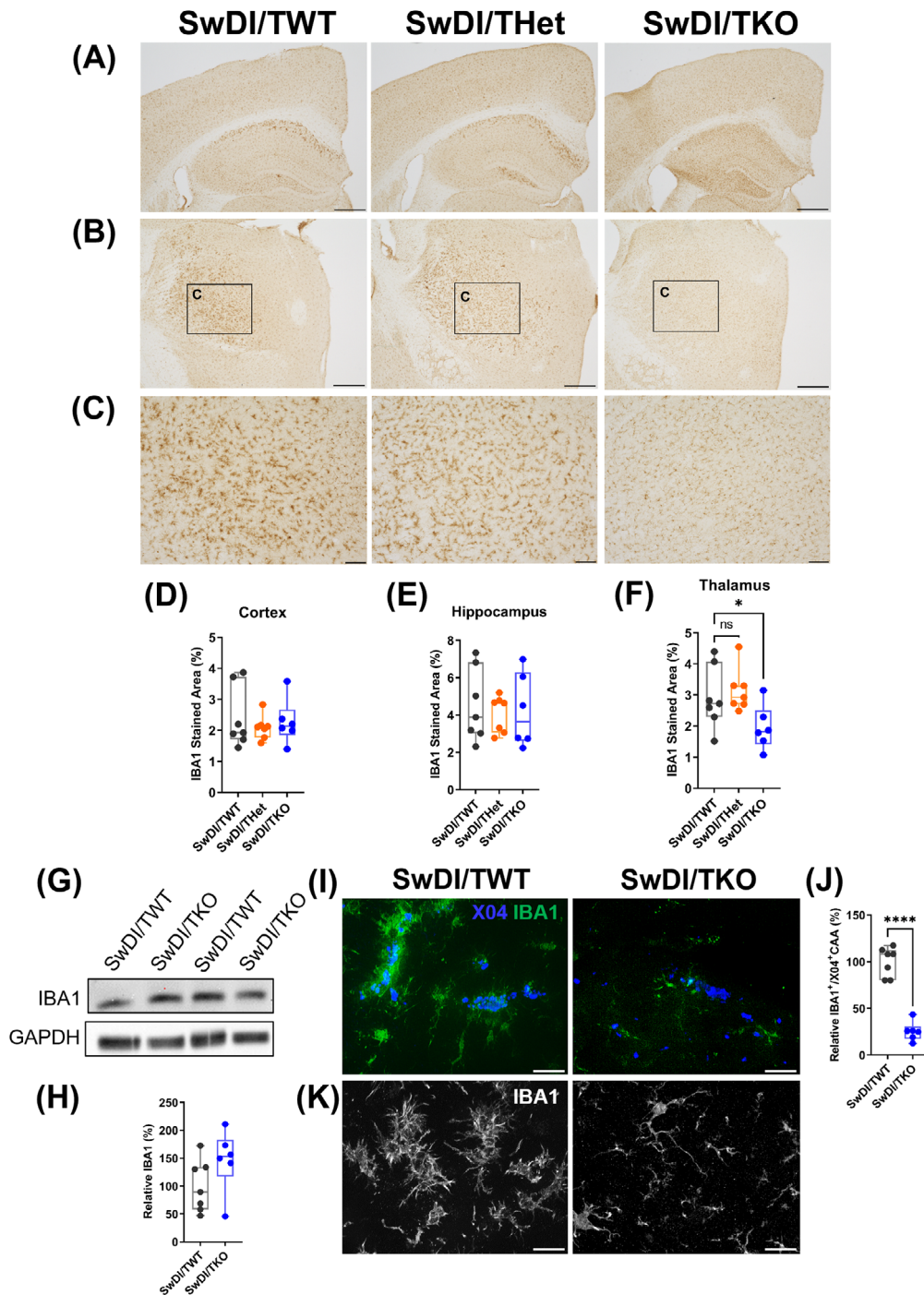
FIGURE 4 *Trem2* deletion reduces microgliosis and CAA-associated microglia in the thalamus. A-C, Representative images of the immunohistochemical staining of microglia by IBA1 in (A) cortex and hippocampus, and (B) thalamus in SwDI/TWT ($n = 7$), SwDI/THet ($n = 7$), and SwDI/TKO ($n = 6$). Scale bars, 500 μm. C, Selected zoomed-in areas from (B). Scale bars, 100 μm. D-F, Quantifications of the immunoreactive area of IBA1 in SwDI/TWT, SwDI/THet, and SwDI/TKO in (D) cortex, (E) hippocampus, and (F) thalamus, respectively. Only in thalamus was a significant decrease observed in IBA1 in SwDI/TKO mice. One-way analysis of variance and Tukey post hoc test. G-H, Immunoblot analysis of IBA1. Representative images of the IBA1 immunoblot (G) and the quantification of IBA1 normalized by GAPDH (H). I-J, CAA-associated microglia in the thalamus. I, Representative images of CAA and microglia stained with X04 and IBA1, respectively, and (J) the quantification. K, Representative images of microglial morphology in thalamus. Microglia adopt a less reactive morphology with longer process and smaller soma in SwDI/TKO than those in SwDI/TWT mice. Unpaired Student's *t*-test, two-tail. *$p < 0.05$, ****$p < 0.0001$. ns, not significant. CAA, cerebral amyloid angiopathy; GAPDH, glyceraldehyde 3-phosphate dehydrogenase; IBA1, ionized calcium-binding adapter molecule 1.
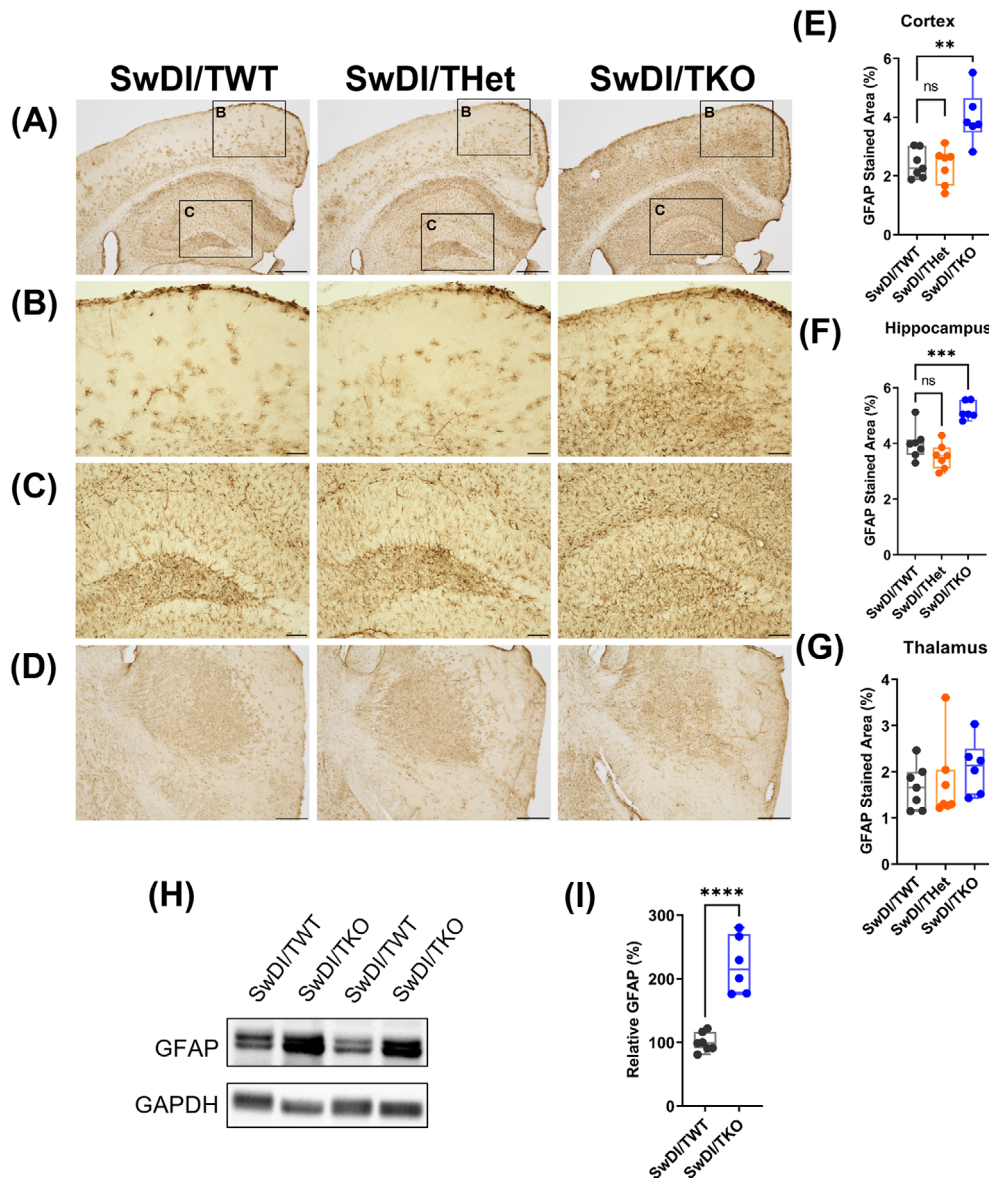
FIGURE 5 *Trem2* deletion aggravates cortical and hippocampal astrocytosis. A, D, Representative images of the immunohistochemical staining of reactive astrocytes by GFAP in (A) cortex, hippocampus, and (D) thalamus in SwDI/TWT ($n = 7$), SwDI/THet ($n = 7$), and SwDI/TKO ($n = 6$). Scale bars, 500 μm. B-C, Selected zoomed-in areas from the representative images of (B) cortex and (C) hippocampus. Scale bars, 100 μm. E-G, Quantifications of the immunoreactive area of GFAP in SwDI/TWT, SwDI/THet, and SwDI/TKO in (E) cortical, (F) hippocampal, and (G) thalamic regions, respectively. One-way analysis of variance and Tukey post hoc test. H-I, Immunoblot analysis of GFAP. Representative images on the GFAP immunoblot (H) and the quantification of GFAP normalized by GAPDH (I). Unpaired Student's t-test, two-tail. $**p < 0.01$, $***p < 0.001$, $****p < 0.0001$. ns, not significant. GAPDH, glyceraldehyde 3-phosphate dehydrogenase; GFAP, glial fibrillary acidic protein.

addition, several pathways pertaining to cell junction maintenance were upregulated in the absence of *Trem2* (Figure 7J). Cluster 1 macrophages are featured by high expression of classic MHC class II genes such as *Cd74*, *H2-Eb1*, and *H2-Ab1* (Figure 7I), indicating an immune reactive status. Although no significant DEGs or pathways were found in SwDI/TKO versus SwDI/TWT, there was a trend of increase in cluster 1 macrophages in SwDI/TKO (Figure S4C-D). Together, these findings showed that perivascular macrophages were differentially activated in the absence of TREM2, likely contributing to pathological changes in SwDI/TKO mice.

3.7 | Vascular cell-type analysis uncovers distinct responses of mural cells and astrocytes to *Trem2* deficiency

To investigate the impact of *Trem*2 deletion on cerebrovascular cells, the snRNA-seq dataset was further analyzed to identify DEGs in vascular cell types (Figure 8A). Comparing SwDI/TKO and SwDI/TWT mice, six upregulated and five downregulated protein-coding DEGs were identified (Figure 8B; Table S2), and pathway analysis indicated their crucial roles in cytoskeleton maintenance (Figure 8C). Furthermore,
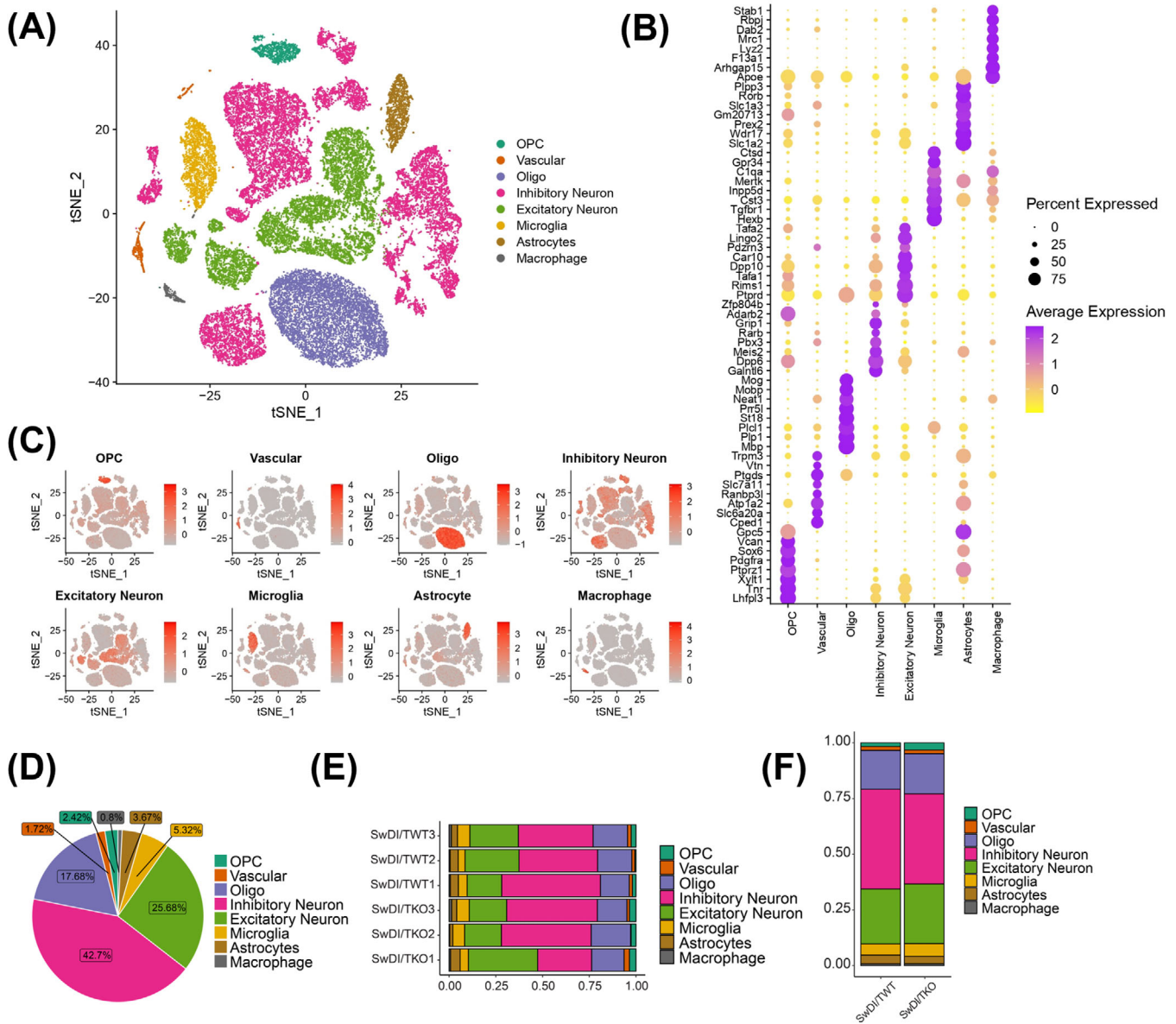
FIGURE 6 snRNA-seq analysis distinguishes major brain-cell types in SwDI/Trem2 mouse brain cortical samples. A, t-SNE plot showing distinguished clusters after integrating dataset from individual samples with eight distinct cell-type identities as determined by algorithm prediction and manual confirmation ($n = 6$ mice total with $n = 3$ mice for each genotype; 36,660 total nuclei). B, Expression of specific markers in every predicted cell type. C, t-SNE visualization of all eight major cell populations showing the average expression of the representative cell type–specific marker genes. Numbers reflect the average number of UMI detected for the representative genes for each cell. D, Pie chart showing the fraction of each cell type after integrating all six samples for both genotypes. E-F, Bar graph showing the fractions of each cell type in (E) individual samples and (F) each genotype averaged as a group. snRNA-seq, single nucleus RNA sequencing; t-SNE, t-distributed stochastic neighbor embedding; UMI, unique molecular identifier.

using recently published subtype-specific vascular marker genes,[59–61] distinct cell clusters were identified, including smooth muscle cells (SMCs), vascular leptomeningeal cells, pericytes, endothelial cells, and astrocytes (Figure 8D-E). Pathway analysis of SwDI/TKO versus SwDI/TWT unveiled divergent responses of vascular cells to *Trem2* deletion. In vascular leptomeningeal and endothelial cells, no significant changes were detected. For SMC, pericytes, and astrocytes, their respective significant pathways were shown in Figure 8F. In both SMC and pericytes, an overall increased cell activity was observed

in SwDI/TKO, including cytoskeleton, cell survival/development and proliferation, and immune function pathways. In addition, in SMC, pathways relevant to smooth muscle contraction were upregulated, and the extracellular matrix pathway was downregulated. As increased microvascular extracellular matrix has been associated with CAA,[62] downregulation of the extracellular matrix was consistent with reduced CAA in SwDI/TKO. Interestingly, while the majority of significant pathways identified in SMC and pericytes were upregulated, almost all significant pathways in vascular-associated astrocytes were
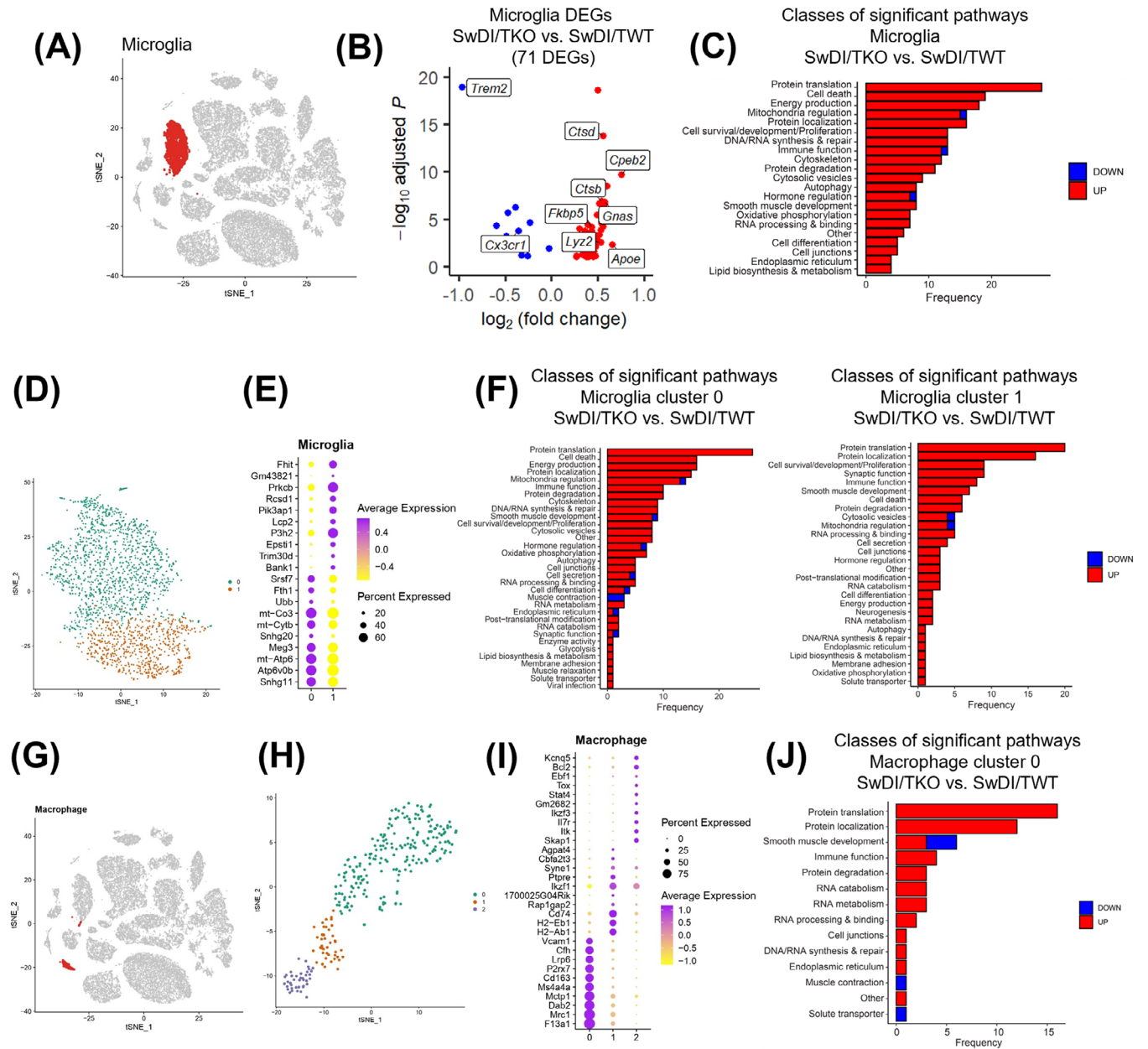
FIGURE 7 *Trem*2 deletion switches microglia and perivascular macrophages to a reactive transcriptomic profile. A, t-SNE plot showing the microglia populations from Figure 6 based on the cell type prediction algorithm. B, Volcano plots showing all 71 significant DEGs (adjusted $p < 0.1$) in microglia of SwDI/TKO versus SwDI/TWT. Stage 1 DAM genes are elevated in SwDI/TKO. C, Bar graph showing different classes of significant pathways (adjusted $p < 0.1$) of SwDI/TKO versus SwDI/TWT in all microglia. Upregulated pathways in red and downregulated pathways in blue. D, t-SNE plot of re-clustered microglia identifying two subclusters, 0 and 1. E, Expression of specific markers in each microglial cluster. F, Bar graphs showing different classes of significant pathways (adjusted $p < 0.1$) of SwDI/TKO versus SwDI/TWT in microglia clusters 0 and 1. Upregulated pathways in red and downregulated pathways in blue. G, t-SNE plot showing the macrophage populations from Figure 6 based on the cell type prediction algorithm. H, t-SNE plot of re-clustered macrophage identifying three subclusters, 0, 1, and 2. I, Expression of specific markers in each macrophage cluster. J, Bar graph showing different classes of significant pathways (adjusted $p < 0.1$) of SwDI/TKO versus SwDI/TWT in macrophage cluster 0. Upregulated pathways in red and downregulated pathways in blue. DAM, disease-associated microglia; DEGs, differentially expressed genes; t-SNE, t-distributed stochastic neighbor embedding.

downregulated in SwDI/TKO mice. These findings indicate that various types of cerebrovascular cells exhibit differential responses to *Trem2* deletion, likely contributing to the pathological phenotypes in SwDI/TKO mice.

4 | DISCUSSION

The present study aimed to fill the gap in knowledge of the role of TREM2 in the pathogenesis of CAA. To achieve this goal, we introduced
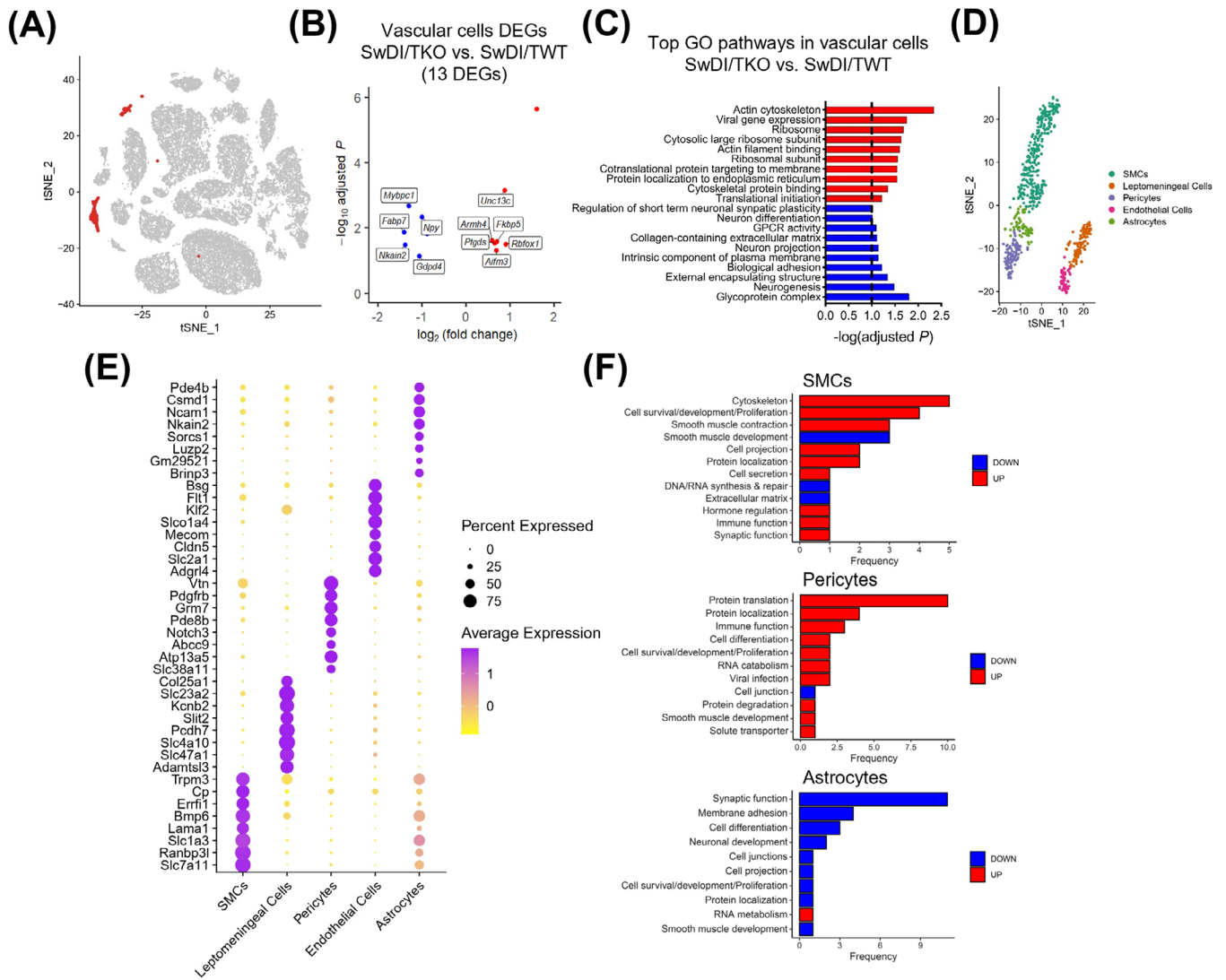
FIGURE 8 Vascular cell-type analysis uncovers distinct responses of mural cells and astrocytes to *Trem2* deficiency. A, t-SNE plot showing the vascular cell populations from Figure 6 based on the cell type prediction algorithm. B, Volcano plots showing all 13 significant DEGs (adjusted $p < 0.1$) in vascular cells of SwDI/TKO versus SwDI/TWT. C, Bar graph showing top 10 up- and downregulated Gene Ontology (GO) significant pathways (adjusted $p < 0.1$) of SwDI/TKO versus SwDI/TWT in all vascular cells. Upregulated pathways in red and downregulated pathways in blue. D, t-SNE plot of re-clustered vascular cells showing five distinct cell types manually identified by reported marker genes. E, Expression of specific markers in each vascular subtype. F, Bar graph showing different classes of significant pathways (adjusted $p < 0.1$) of SwDI/TKO versus SwDI/TWT in smooth muscle cells (SMCs), pericytes, and astrocytes. No significant differential pathways were found in vascular leptomeningeal cells and endothelial cells. DEGs, differentially expressed genes; t-SNE, t-distributed stochastic neighbor embedding.

Trem2 deficiency on the background of SwDI, an established CAA/AD model,[29,43] by breeding SwDI mice with the well-characterized *Trem2* knock-out mice.[30] We performed a comprehensive characterization of the pathologies and molecular signatures of the new SwDI/Trem2 line using immunohistochemical, biochemical, and transcriptomic approaches, and we identified a previously unknown differential effect of TREM2 on modulating parenchymal and vascular amyloid pathology (plaques and CAA). Prior studies have shown that *Trem2* deficiency affects overall amyloid pathology in a disease stage–dependent manner, generally with an increase in total amyloid in the late stage but a decrease or no change in the earlier phase.[4–9] However, those studies were conducted in Aβ42-enriched, parenchymal plaques–dominant

mouse models. In the present study, we used the Aβ40-enriched, CAA-prone SwDI/Trem2 mice at 16 months, when both amyloid plaques and CAA are usually well developed in SwDI mice at this age,[43] to assess the function of TREM2.

Consistent with previous findings from other AD models at a late disease stage, loss of *Trem2* led to a robust increase in overall amyloid load in the cortex, hippocampus, and thalamus in SwDI mice (Figure 1). Interestingly, haplodeficiency of *Trem2* was not sufficient to modulate cerebral Aβ deposition in SwDI mice, which is consistent with the results in APPPS1-21 mice,[8] although a dose-dependent effect of *Trem2* has been reported in 5XFAD mice.[4] Because of the fibrillar nature of Aβ in CAA, in addition to Aβ immunostaining,

methoxy-X04 staining was used to assess the amount of amyloid fibrils in SwDI/Trem2 mice. The results showed a significant increase of fibrillar Aβ in the three regions in SwDI/TKO, similar to total amyloid load assessed by Aβ immunostaining; however, unexpectedly, loss of Trem2 led to marked reduction of CAA, in particular in the thalamus where CAA is predominantly located in SwDI mice (Figure 3). These intriguing findings, for the first time, reveal the differential impact of Trem2 deficiency on parenchymal and vascular amyloidosis.

Subsequent quantification of Aβ species was performed with Aβ40- and Aβ42-specific ELISA to understand their contributions to the discordant parenchymal Aβ deposition and CAA. The results showed a significant increase in both Aβ40 and Aβ42 in either soluble or insoluble fractions of the total brain homogenates in SwDI/TKO mice. Importantly, the Aβ40/Aβ42 ratio was also elevated, indicating that Aβ40 was increased more than Aβ42. Because the increase of Aβ40 promotes CAA, this would predict exacerbation rather than diminishment of CAA as observed in SwDI/TKO mice. This paradoxical finding might be the result of Aβ redistribution. As reported in a study with a bigenic model from crossing SwDI with 5XFAD, an aggressive plaque-rich model,[63] early parenchymal fibrillar amyloid plaques originated from 5XFAD act as a scaffold to capture CAA composed by vasculotropic Dutch/Iowa mutant Aβ and promote its local assembly and deposition into parenchymal plaques, hence precluding microvascular amyloid formation. Based on the finding that loss of or dysfunctional TREM2 boosts amyloid seeding in the early stages,[44,64] the shift from CAA to parenchymal plaques was likely caused by increased amyloid seeding in the brain parenchyma of SwDI/TKO mice. The overall increase of both total and fibrillar Aβ deposition in various brain regions observed in SwDI mice supports this notion. Interestingly, recent studies found that depletion of microglia led to a decrease in parenchymal plaques but an increase in CAA in 5XFAD mice.[26,65] These findings corroborate the role of microglia in the dynamics of parenchymal and vascular Aβ deposition, and in the meantime demonstrate that lack of microglia is not equivalent to lack of TREM2 and other microglial functions are likely responsible for the opposite outcome. In addition, the intrinsic differences between the mouse models (Aβ40-dominant SwDI vs. Aβ42-dominant 5XFAD) and the disease stages may also contribute to the discrepancy. How depletion of microglia modulates the parenchymal and vascular Aβ distribution in SwDI mice awaits further investigation.

In SwDI/TKO mice, CAA-associated IBA1+ microglia were reduced compared to SwDI/TWT, consistent with previous studies reporting reduced plaque-associated microglia in other Trem2-deficient AD mice.[4-9,32,44] Notably, in the brain cortex where diffused plaques were prevalent, there was no change in the extent of microgliosis by IBA1 staining (Figure 4D) in the absence of Trem2. This could be attributed to the fact that the microglial activation in the cortex of SwDI mice is limited in the first place due to the scarce Aβ fibrillar pathology.[43,66] Although Trem2 deletion led to an increase in fibrillar Aβ, Trem2-deficient microglia failed to respond in SwDI/TKO mice, which is supported by snRNA-seq data.

Of note, brain regional similarities and differences in pathology were observed after Trem2 deletion. In the SwDI model, Aβ deposits were first found in the subiculum, hippocampus, and cortex at $\approx$ 3 months followed by the olfactory bulb and thalamic region at $\approx$ 6 months.[29] Subiculum and thalamus are the two CAA-prone regions in SwDI and are more susceptible to microgliosis and astrocytosis than the cortex along the course of pathological development in SwDI mice from 6 to 12 months.[43] In the present study, Trem2 deletion led to a significant exacerbation of the overall amyloid pathology in three brain regions including the cortex, hippocampus, and thalamus in SwDI mice at 16 months (Figures 1 and 3). However, microgliosis was reduced in the thalamus (Figure 4), associated with a reduction of CAA where microglia adopted a less reactive and dystrophic morphology (Figure 4K), whereas astrocytosis was increased in the cortex and hippocampus with no change in the thalamus (Figure 5), indicating that astrocytes responded more to parenchymal Aβ deposition than to CAA. Importantly, the impact of TREM2 on brain region–specific immune response and plaque microenvironment has also been observed in human AD. A recent report showed that dystrophic microglia were most abundant in the subiculum region in human brains across all AD stages, especially in patients harboring risk variants of TREM2.[67] Taken together, the regional similarities and differences in brain pathology observed in SwDI/TKO mice most likely resulted from the distribution and nature of the amyloid deposition (plaques vs. CAA) and corresponding cellular responses.

Transcriptomic analysis showed that microglia displayed a partially reactive profile, trapped in the intermediate state of DAM Stage 1 in SwDI/TKO compared to SwDI/TWT, without being fully activated to the DAM Stage 2 as reported.[9,49,50,64] These results are consistent with the notion that Stage 1 DAM genes are Trem2 independent whereas Stage 2 DAM genes are Trem2 dependent.[49] Pathway analysis also revealed a stressed state of microglia in SwDI/TKO, with overwhelming upregulation of protein synthesis, cell death, energy production, immune response, and lipid biosynthesis and metabolism pathways. Interestingly, it has been reported that Trem2 deficiency leads to induced autophagy but curtails biosynthetic and energetic metabolism in 5XFAD mice.[68] Here, we found both autophagy and energy production pathways were upregulated in SwDI/TKO mice, indicating both overlapping and divergent responses in different AD models.

Further, we identified a PVM subcluster from the macrophage population through snRNA-seq analysis. The role of perivascular macrophages in cerebrovascular function is well recognized. In the homeostatic state, PVMs in the brain are beneficial, involving in the clearance of waste products from the cerebral parenchyma and in the regulation of the cerebrospinal fluid (CSF) flow through extracellular matrix.[69,70] However, under pathological conditions including AD, PVMs could be a double-edged sword, depending on the disease stage. On one hand, PVMs facilitate amyloid clearance at the vascular level.[54,71] On the other hand, PVMs exacerbate Aβ-induced neurovascular dysfunction by providing reactive oxygen species.[55] In addition, PVMs contribute to the degradation of extracellular matrix that in turn regulates the diameter of the perivascular space and increases CSF flow.[70,72]

Pathway analysis showed that PVMs were differentially activated in SwDI/TKO mice. In addition to upregulation of protein synthesis and immune function pathways as in microglia, cell junction pathways were upregulated in the absence of *Trem2* (Figure 7J), indicating a potential impact on BBB integrity. In addition, snRNA-seq analyses in vascular cells showed that mural cells (SMCs and pericytes) were activated, whereas vascular-associated astrocytes were suppressed in SwDI/TKO mice. Because these cells are involved in the regulation of neurovascular structure and functions,[73–75] transcriptomic changes in each of the cell types likely contributed to the pathological phenotype in SwDI/TKO mice. The results also demonstrate that lack of *Trem2* not only affects microglia but also modifies the response of various other cell types in the brain.

Our findings offer an important perspective on ongoing efforts developing TREM2 agonists as a potential therapeutic for AD. Recent results from the clinical trial with the TREM2-activating antibody AL002 have shown that ARIAs are one of the most prevalent and severe adverse events, as observed with anti-Aβ immunotherapies.[76] This observation is consistent with our finding that TREM2 plays a crucial role in the formation of CAA. Antibody-induced activation of TREM2 may lead to the worsening of CAA, thus likely contributing to the aggravation of ARIAs in clinical trials with TREM2 agonists. These findings suggest that it may be necessary for TREM2-targeting therapies to balance the activation and inhibition of TREM2 to achieve optimal outcomes.

Overall, our study provides the first evidence that TREM2 differentially modulates parenchymal and cerebrovascular amyloid pathology in a CAA-prone mouse model of AD. Despite the overall increase of amyloid load in the brain, lack of *Trem2* diminishes CAA, the well-recognized culprit for cerebrovascular dysfunction, including the severe side effect of ARIAs associated with anti-Aβ and TREM2-activating immunotherapies. Therefore, our findings may have significant implications for both TREM2- and Aβ-targeting therapies for AD.

CONFLICT OF INTEREST STATEMENT

All authors declare no competing interests. Author disclosures are available in the supporting information.

CONSENT STATEMENT

This study did not involve human subjects; consent was not necessary.

DATA AVAILABILITY STATEMENT

The raw snRNA-seq datasets generated in this study are available in the Gene Expression Omnibus repository (GEO Series accession number GSE244286).

ORCID

Rui Zhong https://orcid.org/0000-0002-8936-6652
Ling Li https://orcid.org/0000-0002-9245-7387

REFERENCES

1. Jonsson T, Stefansson H, Steinberg S, et al. Variant of TREM2 associated with the risk of Alzheimer's disease. *N Engl J Med*. 2013;368(2):107-116. doi: 10.1056/NEJMoa1211103
2. Guerreiro R, Wojtas A, Bras J, et al. TREM2 variants in Alzheimer's disease . *N Engl J Med*. 2013;368(2):117-127. doi: 10.1056/NEJMOA1211851/SUPPL_FILE/NEJMOA1211851_DISCLOSURES.PDF
3. Qu W, Li L. Loss of TREM2 confers resilience to synaptic and cognitive impairment in aged mice. *J Neurosci*. 2020;40(50):9552-9563. doi: 10.1523/JNEUROSCI.2193-20.2020
4. Wang Y, Cella M, Mallinson K, et al. TREM2 lipid sensing sustains the microglial response in an Alzheimer's disease model. *Cell*. 2015;160(6):1061-1071. doi: 10.1016/j.cell.2015.01.049
5. Jay TR, Miller CM, Cheng PJ, et al. TREM2 deficiency eliminates TREM2+ inflammatory macrophages and ameliorates pathology in Alzheimer's disease mouse models. *J Exp Med*. 2015;212(3):287-295. doi: 10.1084/jem.20142322
6. Wang Y, Ulland TK, Ulrich JD, et al. TREM2-mediated early microglial response limits diffusion and toxicity of amyloid plaques. *J Exp Med*. 2016;213(5):667-675. doi: 10.1084/jem.20151948
7. Jay TR, Hirsch AM, Broihier ML, et al. Disease progression-dependent effects of TREM2 deficiency in a mouse model of Alzheimer's disease. *J Neurosci*. 2017;37(3):637-647. doi: 10.1523/JNEUROSCI.2110-16.2016
8. Ulrich JD, Finn MB, Wang Y, et al. Altered microglial response to Aβ plaques in APPPS1-21 mice heterozygous for TREM2. *Mol Neurodegener*. 2014;9(1):20. doi: 10.1186/1750-1326-9-20
9. Krasemann S, Madore C, Cialic R, et al. The TREM2-APOE pathway drives the transcriptional phenotype of dysfunctional microglia in neurodegenerative diseases. *Immunity*. 2017;47(3):566-581.e9. doi: 10.1016/j.immuni.2017.08.008
10. Joshi P, Riffel F, Kumar S, et al. TREM2 modulates differential deposition of modified and non-modified Aβ species in extracellular plaques and intraneuronal deposits. *Acta Neuropathol Commun*. 2021;9(1):1-22. doi: 10.1186/S40478-021-01263-X/FIGURES/7
11. Viswanathan A, Greenberg SM. Cerebral amyloid angiopathy in the elderly. *Ann Neurol*. 2011;70(6):871-880. doi: 10.1002/ANA.22516
12. Greenberg SM, Bacskai BJ, Hernandez-Guillamon M, Pruzin J, Sperling R, van Veluw SJ. Cerebral amyloid angiopathy and Alzheimer disease — one peptide, two pathways. *Nat Rev Neurol*. 2020;16(1):30-42. doi: 10.1038/s41582-019-0281-2
13. Pfeifer LA, White LR, Ross GW, Petrovitch H, Launer LJ. Cerebral amyloid angiopathy and cognitive function: The HAAS autopsy study. *Neurology*. 2002;58(11):1629-1634. doi: 10.1212/WNL.58.11.1629
14. Gandy S. News & views: anti-amyloid antibodies and novel emerging approaches to Alzheimer's disease in 2023. *Mol Neurodegener*. 2023;18(1):1-3. doi: 10.1186/S13024-023-00656-X
15. Karran E, De Strooper B. The amyloid hypothesis in Alzheimer disease: new insights from new therapeutics. *Nat Rev Drug Discov 2022*.

Published online February 17, 2022:1-13. doi: 10.1038/s41573-022-00391-w

16. O'Brien RJ, Wong PC. Amyloid precursor protein processing and Alzheimer's disease. *Annu Rev Neurosci.* https://doi-org.ezp1.lib.umn.edu/101146/annurev-neuro-061010-113613. 2011;34:185-204. doi: 10.1146/ANNUREV-NEURO-061010-113613

17. Mullan M, Crawford F, Axelman K, et al. A pathogenic mutation for probable Alzheimer's disease in the APP gene at the N–terminus of β–amyloid. *Nat Genet.* 1992;1(5):345-347. doi: 10.1038/ng0892-345

18. Levy E, Carman MD, Fernandez-Madrid IJ, et al. Mutation of the Alzheimer's disease amyloid gene in hereditary cerebral hemorrhage, Dutch Type. *Science (80-).* 1990;248(4959):1124-1126. doi: 10.1126/SCIENCE.2111584

19. Grabowski TJ, Cho HS, Vonsattel JPG, William Rebeck G, Greenberg SM. Novel amyloid precursor protein mutation in an Iowa family with dementia and severe cerebral amyloid angiopathy. *Ann Neurol.* 2001;49(6):697-705. doi: 10.1002/ANA.1009

20. Miller DL, Papayannopoulos IA, Styles J, et al. Peptide compositions of the cerebrovascular and senile plaque core amyloid deposits of Alzheimer's disease. *Arch Biochem Biophys.* 1993;301(1):41-52. doi: 10.1006/abbi.1993.1112

21. Gravina SA, Ho L, Eckman CB, et al. Amyloid β protein (Aβ) in Alzheimeri's disease brain. *J Biol Chem.* 1995;270(13):7013-7016. doi: 10.1074/jbc.270.13.7013

22. Govindpani K, McNamara LG, Smith NR, et al. Vascular dysfunction in Alzheimer's disease: a prelude to the pathological process or a consequence of it? *J Clin Med.* 2019;8(5):651. doi: 10.3390/jcm8050651

23. Korte N, Nortley R, Attwell D. Cerebral blood flow decrease as an early pathological mechanism in Alzheimer's disease. *Acta Neuropathol.* 2020;140(0123456789):793. doi: 10.1007/s00401-020-02215-w

24. Weller RO, Subash M, Preston SD, Mazanti I, Carare RO. SYMPOSIUM: clearance of Aβ from the brain in Alzheimer's disease: perivascular drainage of amyloid-β peptides from the brain and its failure in cerebral amyloid angiopathy and Alzheimer's disease. *Brain Pathol.* 2008;18(2):253-266. doi: 10.1111/J.1750-3639.2008.00133.X

25. Chen X, Liu X, Koundal S, et al. Cerebral amyloid angiopathy is associated with glymphatic transport reduction and time-delayed solute drainage along the neck arteries. *Nat Aging.* 2022;2(3):214-223. doi: 10.1038/s43587-022-00181-4

26. Kiani Shabestari S, Morabito S, Danhash EP, et al. Absence of microglia promotes diverse pathologies and early lethality in Alzheimer's disease mice. *Cell Rep.* 2022;39(11):110961. doi: 10.1016/J.CELREP.2022.110961/ATTACHMENT/AE2B78A4-554F-401E-8B38-4D8D2BFBF226/MMC1.PDF

27. Delaney C, Farrell M, Doherty CP, et al. Attenuated CSF-1R signalling drives cerebrovascular pathology. *EMBO Mol Med.* 2021;13(2):e12889. doi:10.15252/EMMM.202012889

28. Scholtzova H, Do E, Dhakal S, et al. Innate immunity stimulation via toll-like receptor 9 ameliorates vascular amyloid pathology in Tg-SwDI mice with associated cognitive benefits. *J Neurosci.* 2017;37(4):936-959. doi: 10.1523/JNEUROSCI.1967-16.2016

29. Davis J, Xu F, Deane R, et al. Early-onset and robust cerebral microvascular accumulation of amyloid β-protein in transgenic mice expressing low levels of a vasculotropic dutch/iowa mutant form of amyloid β-protein precursor. *J Biol Chem.* 2004;279(19):20296-20306. doi: 10.1074/JBC.M312946200

30. Turnbull IR, Gilfillan S, Cella M, et al. Cutting edge: TREM-2 attenuates macrophage activation. *J Immunol.* 2006;177(6):3520-3524. doi: 10.4049/JIMMUNOL.177.6.3520

31. Qu W, Jeong A, Zhong R, Thieschafer JS, Gram A, Li L. Deletion of small GTPase H-ras rescues memory deficits and reduces amyloid plaque-associated dendritic spine loss in transgenic Alzheimer's mice. *Mol Neurobiol.* 2023;60:495-511. doi: 10.1007/S12035-022-03082-0

32. Meilandt WJ, Ngu H, Gogineni A, et al. TREM2 deletion reduces late-stage amyloid plaque accumulation, elevates the Aβ42:Aβ40 ratio, and exacerbates axonal dystrophy and dendritic spine loss in the PS2ApP Alzheimer's mouse model. *J Neurosci.* 2020;40(9):1956-1974. doi: 10.1523/JNEUROSCI.1871-19.2019

33. Jeong A, Cheng S, Zhong R, Bennett DA, Bergö MO, Li L. Protein farnesylation is upregulated in Alzheimer's human brains and neuron-specific suppression of farnesyltransferase mitigates pathogenic processes in Alzheimer's model mice. *Acta Neuropathol Commun.* 2021;9(1):1-24. doi: 10.1186/S40478-021-01231-5

34. Park YG, Sohn CH, Chen R, et al. Protection of tissue physico-chemical properties using polyfunctional crosslinkers. *Nat Biotechnol.* 2018;37(1):73. doi: 10.1038/nbt.4281

35. Kim SY, Cho JH, Murray E, et al. Stochastic electrotransport selectively enhances the transport of highly electromobile molecules. *Proc Natl Acad Sci U S A.* 2015;112(46):E6274-E6283. doi: 10.1073/PNAS.1510133112/-/DCSUPPLEMENTAL

36. Murray E, Cho JH, Goodwin D, et al. Simple, scalable proteomic imaging for high-dimensional profiling of intact systems. *Cell.* 2015;163(6):1500-1514. doi: 10.1016/j.cell.2015.11.025

37. Dobin A, Davis CA, Schlesinger F, et al. STAR: ultrafast universal RNA-seq aligner. *Bioinformatics.* 2013;29(1):15-21. doi: 10.1093/BIOINFORMATICS/BTS635

38. Butler A, Hoffman P, Smibert P, Papalexi E, Satija R. Integrating single-cell transcriptomic data across different conditions, technologies, and species. *Nat Biotechnol.* 2018;36(5):411-420. doi: 10.1038/nbt.4096

39. McGinnis CS, Murrow LM, Gartner ZJ. DoubletFinder: doublet detection in single-cell RNA sequencing data using artificial nearest neighbors. *Cell Syst.* 2019;8(4):329-337.e4. doi: 10.1016/J.CELS.2019.03.003

40. Korsunsky I, Millard N, Fan J, et al. Fast, sensitive and accurate integration of single-cell data with Harmony. *Nat Methods.* 2019;16(12):1289-1296. doi: 10.1038/s41592-019-0619-0

41. Yao Z, van Velthoven CTJ, Nguyen TN, et al. A taxonomy of transcriptomic cell types across the isocortex and hippocampal formation. *Cell.* 2021;184(12):3222-3241.e26. doi: 10.1016/J.CELL.2021.04.021

42. Tasic B, Menon V, Nguyen TN, et al. Adult mouse cortical cell taxonomy revealed by single cell transcriptomics. *Nat Neurosci.* 2016;19(2):335-346. doi: 10.1038/nn.4216

43. Miao J, Xu F, Davis J, Otte-Höller I, Verbeek MM, Van Nostrand WE. Cerebral microvascular amyloid β protein deposition induces vascular degeneration and neuroinflammation in transgenic mice expressing human vasculotropic mutant amyloid β precursor protein. *Am J Pathol.* 2005;167(2):505-515. doi: 10.1016/S0002-9440(10)62993-8

44. Parhizkar S, Arzberger T, Brendel M, et al. Loss of TREM2 function increases amyloid seeding but reduces plaque-associated ApoE. *Nat Neurosci.* 2019;22(2):191-204. doi: 10.1038/s41593-018-0296-9

45. McKenzie AT, Wang M, Hauberg ME, et al. Brain cell type specific gene expression and co-expression network architectures. *Sci Reports.* 2018;8(1):1-19. doi: 10.1038/s41598-018-27293-5

46. Zeisel A, Hochgerner H, Lönnerberg P, et al. Molecular architecture of the mouse nervous system. *Cell.* 2018;174(4):999-1014.e22. doi: 10.1016/J.CELL.2018.06.021

47. Ximerakis M, Lipnick SL, Innes BT, et al. Single-cell transcriptomic profiling of the aging mouse brain. *Nat Neurosci.* 2019;22(10):1696-1708. doi: 10.1038/s41593-019-0491-3

48. Grubman A, Chew G, Ouyang JF, et al. A single-cell atlas of entorhinal cortex from individuals with Alzheimer's disease reveals cell-type-specific gene expression regulation. *Nat Neurosci.* 2019;22(12):2087-2097. doi: 10.1038/s41593-019-0539-4

49. Keren-Shaul H, Spinrad A, Weiner A, et al. A unique microglia type associated with restricting development of Alzheimer's disease. *Cell.* 2017;169(7):1276-1290.e17. doi: 10.1016/j.cell.2017.05.018

50. Zhou Y, Song WM, Andhey PS, et al. Human and mouse single-nucleus transcriptomics reveal TREM2-dependent and TREM2-independent

cellular responses in Alzheimer's disease. *Nat Med.* 2020;26(1):131-142. doi: 10.1038/s41591-019-0695-9

51. Li RY, Qin Q, Yang HC, et al. TREM2 in the pathogenesis of AD: a lipid metabolism regulator and potential metabolic therapeutic target. *Mol Neurodegener.* 2022;17(1):1-19. doi: 10.1186/S13024-022-00542-Y

52. Kim WK, Alvarez X, Fisher J, et al. CD163 identifies perivascular macrophages in normal and viral encephalitic brains and potential precursors to perivascular macrophages in blood. *Am J Pathol.* 2006;168(3):822-834. doi: 10.2353/ajpath.2006.050215

53. Holder GE, McGary CM, Johnson EM, et al. Expression of the mannose receptor CD206 in HIV and SIV encephalitis: a phenotypic switch of brain perivascular macrophages with virus infection. *J Neuroimmune Pharmacol.* 2014;9(5):716-726. doi: 10.1007/S11481-014-9564-Y/FIGURES/6

54. Thanopoulou K, Fragkouli A, Stylianopoulou F, Georgopoulos S. Scavenger receptor class B type i (SR-BI) regulates perivascular macrophages and modifies amyloid pathology in an Alzheimer mouse model. *Proc Natl Acad Sci U S A.* 2010;107(48):20816-20821. doi: 10.1073/pnas.1005888107

55. Park L, Uekawa K, Garcia-bonilla L, et al. Brain perivascular macrophages initiate the neurovascular dysfunction of Alzheimer Aβ peptides. *Circ Res.* 2017;121(3):258-269. doi: 10.1161/CIRCRESAHA.117.311054

56. Wang L. FKBP51 regulation of AKT/protein kinase B phosphorylation. *Curr Opin Pharmacol.* 2011;11(4):360-364. doi: 10.1016/J.COPH.2011.03.008

57. Zannas AS, Jia M, Hafner K, et al. Epigenetic upregulation of FKBP5 by aging and stress contributes to NF-κB-driven inflammation and cardiovascular risk. *Proc Natl Acad Sci U S A.* 2019;166(23):11370-11379. doi: 10.1073/PNAS.1816847116/SUPPL_FILE/PNAS.1816847116.SD10.XLSX

58. Sayed FA, Kodama L, Fan L, et al. AD-linked R47H-TREM2 mutation induces disease-enhancing microglial states via AKT hyperactivation. *Sci Transl Med.* 2021;13(622):3947. doi: 10.1126/SCITRANSLMED.ABE3947/SUPPL_FILE/SCITRANSLMED.ABE3947_MOVIE_S1.ZIP

59. Vanlandewijck M, He L, Mäe MA, et al. A molecular atlas of cell types and zonation in the brain vasculature. *Nat.* 2018;554(7693):475-480. doi: 10.1038/nature25739

60. Barisano G, Kisler K, Wilkinson B, et al. A "multi-omics" analysis of blood–brain barrier and synaptic dysfunction in APOE4 mice. *J Exp Med.* 2022;219(11):e20221137. doi: 10.1084/JEM.20221137

61. Lee S, Devanney NA, Golden LR, et al. APOE modulates microglial immunometabolism in response to age, amyloid pathology, and inflammatory challenge. *Cell Rep.* 2023;42(3):112196. doi: 10.1016/J.CELREP.2023.112196

62. Damodarasamy M, Vernon RB, Pathan JL, et al. The microvascular extracellular matrix in brains with Alzheimer's disease neuropathologic change (ADNC) and cerebral amyloid angiopathy (CAA). *Fluids Barriers CNS.* 2020;17(1):1-11. doi: 10.1186/S12987-020-00219-Y/FIGURES/5

63. Xu F, Kotarba AME, Ou-Yang MH, et al. Early-onset formation of parenchymal plaque amyloid abrogates cerebral microvascular amyloid accumulation in transgenic mice. *J Biol Chem.* 2014;289(25):17895-17908. doi: 10.1074/jbc.M113.536565

64. Zhao N, Qiao W, Li F, et al. Elevating microglia TREM2 reduces amyloid seeding and suppresses disease-associated microglia. *J Exp Med.* 2022;219(12):e20212479. doi: 10.1084/JEM.20212479

65. Spangenberg E, Severson PL, Hohs LA, et al. Sustained microglial depletion with CSF1R inhibitor impairs parenchymal plaque development in an Alzheimer's disease model. *Nat Commun.* 2019;10(1):3758. Published online 2019:1-21. doi: 10.1038/s41467-019-11674-z

66. Fan R, Xu F, Lou Previti M, et al. Minocycline reduces microglial activation and improves behavioral deficits in a transgenic model of cerebral microvascular amyloid. *J Neurosci.* 2007;27(12):3057-3063. doi: 10.1523/JNEUROSCI.4371-06.2007

67. Prokop S, Miller KR, Labra SR, et al. Impact of TREM2 risk variants on brain region-specific immune activation and plaque microenvironment in Alzheimer's disease patient brain samples. *Acta Neuropathol.* 2019;138(4):613-630. doi: 10.1007/S00401-019-02048-2/FIGURES/8

68. Ulland TK, Song WM, Huang SC, et al. TREM2 maintains microglial metabolic fitness in Alzheimer's disease. *Cell.* 2017;170(4):649-656.e13. doi: 10.1016/j.cell.2017.07.023

69. Kida S, Steart PV, Zhang ET, Weller RO. Perivascular cells act as scavengers in the cerebral perivascular spaces and remain distinct from pericytes, microglia and macrophages. *Acta Neuropathol.* 1993;85(6):646-652. doi: 10.1007/BF00334675/METRICS

70. Drieu A, Du S, Storck SE, et al. Parenchymal border macrophages regulate the flow dynamics of the cerebrospinal fluid. *Nature.* 2022;611(7936):585-593. doi: 10.1038/s41586-022-05397-3

71. Hawkes CA, McLaurin J. Selective targeting of perivascular macrophages for clearance of β-amyloid in cerebral amyloid angiopathy. *Proc Natl Acad Sci U S A.* 2009;106(4):1261-1266. doi: 10.1073/pnas.0805453106

72. Ahn JH, Cho H, Kim JH, et al. Meningeal lymphatic vessels at the skull base drain cerebrospinal fluid. *Nat.* 2019;572(7767):62-66. doi: 10.1038/s41586-019-1419-5

73. Hill RA, Tong L, Yuan P, et al. Regional blood flow in the normal and ischemic brain is controlled by arteriolar smooth muscle cell contractility and not by capillary pericytes article regional blood flow in the normal and ischemic brain is controlled by arteriolar smooth muscle cell co. *Neuron.* 2015;87(1):95-110. doi: 10.1016/j.neuron.2015.06.001

74. Sweeney MD, Ayyadurai S, Zlokovic B V. Pericytes of the neurovascular unit: key functions and signaling pathways. *Nat Neurosci.* 2016;19(6):771-783. doi: 10.1038/nn.4288

75. Takano T, Tian GF, Peng W, et al. Astrocyte-mediated control of cerebral blood flow. *Nat Neurosci.* 2005;9(2):260-267. doi: 10.1038/nn1623

76. AlzForum. AL002. Published 2023. Accessed May 20, 2024. https://www.alzforum.org/therapeutics/al002

SUPPORTING INFORMATION

Additional supporting information can be found online in the Supporting Information section at the end of this article.